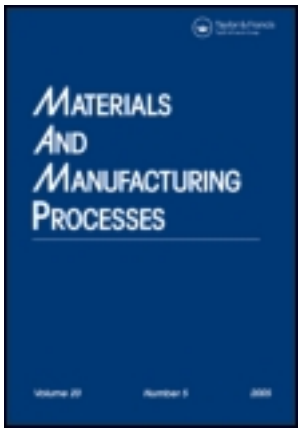

Materials and Manufacturing Processes
Publication details, including instructions for authors and subscription information:
http://www.tandfonline.com/loi/lmmp20

Multiobjective Optimization of Experimental and Simulated Residual Stresses in Turning of Nickel-Alloy IN100

Durul Ulutan [a] & Tuğrul Özel [a]

[a] Department of Industrial and Systems Engineering , Rutgers University , Piscataway , New Jersey , USA

Accepted author version posted online: 16 Aug 2012.

To cite this article: Durul Ulutan & Turul zel (2013) Multiobjective Optimization of Experimental and Simulated Residual Stresses in Turning of Nickel-Alloy IN100, Materials and Manufacturing Processes, 28:7, 835-841, DOI: 10.1080/10426914.2012.718474

To link to this article: http://dx.doi.org/10.1080/10426914.2012.718474

Materials and Manufacturing Processes, 28: 835–841, 2013

ISSN: 1042-6914 print/1532-2475 online
DOI: 10.1080/10426914.2012.718474

Taylor & Francis
Taylor & Francis Group

Multiobjective Optimization of Experimental and Simulated Residual Stresses in Turning of Nickel-Alloy IN100

Durul Ulutan and Tuğrul Özel

Department of Industrial and Systems Engineering, Rutgers University, Piscataway, New Jersey, USA

In this study, physics-based simulations are utilized to predict the forces and residual stresses induced during machining, and the results were validated using the experimental measurements. Physics-based simulations also involve uncertainty in the predicted values that can be represented as expected value and variance of the predictions. These predictions are inputted to a multiobjective optimization methodology to select the optimal machining parameters where competing or conflicting objectives constitute hurdles in the decision-making of the manufacturing plans. The objectives are chosen as related to residual stress measurements and predictions. Multiobjective particle swarm optimization (PSO) procedure is employed in optimizing process parameters. Objectives are solved for minimizing tensile residual stresses on the surface, maximizing peak compressive residual stresses, and minimizing the variance of these variables in order to increase certainty in the predictions. The optimum machining parameters corresponding to this multiobjective optimization are represented in both objective function and decision variable spaces.

Keywords Machining; Nickel-based alloy; Particle swarm optimization; Residual stress.

Introduction

In the aerospace industry, nickel-based alloys are frequently used for critical structural components, especially due to their higher strength at both low and high temperatures, and higher wear and chemical degradation resistance. However, because of their unfavorable thermal properties, deformation and friction-induced microstructural changes prevent the end products from having good surface integrity properties. In addition to surface roughness, microhardness changes, and microstructural alterations, the machining-induced residual stress profiles of titanium and nickel-based alloys contribute in the surface integrity of these products. Machining processes often utilized as the finishing process in the process chain of producing nickel-based super alloyed end products [1, 2]. Process-induced residual stress of surface integrity is a critical and determining factor of such products' fatigue life. Optimizing process parameters for most favorable residual stress profile is a great interest to the industry. Therefore, it is essential to create a comprehensive method that predicts the residual stress outcomes of machining processes, and understand how machining parameters or tool parameters affect the machining-induced residual stresses [3]. For this purpose, face turning experiments are conducted to obtain machining-induced residual stress measurements on the nickel alloy disk specimen. At the same machining configuration and conditions, physics-based finite element simulations have been designed and performed in order to predict machining-induced residual stress profiles with experimental validations.

Received May 29, 2012; Accepted July 6, 2012

Address correspondence to Tuğrul Özel, Department of Industrial and Systems Engineering Rutgers University, Piscataway, NJ 08854, USA; E-mail: ozel@rutgers.edu

Experimental work

n the machining (face turning) experiments, IN100, a nickel-based alloy material, is used. This alloy is manufactured via powder metallurgy route with a chemical composition of 18.3% Co, 12.3% Cr, 4.9% Al, 4.3% Ti, 3.3% Mo, 0.7% V, 0.1% Fe, 0.06% C, 0.02% B, 0.02% Zr and Ni balance. The alloy material was isostatically pressed, and cylindrical billets were formed. Disks with 113 mm diameter were cut from the billet with wire electrical discharge machining (WEDM) process. IN100 disks were machined in a face-turning operation using TPG432 insert type tool (nose radius of $r_\varepsilon = 0.8$ mm and relief angle of $\alpha = 11°$) in a CNC machining center without any coolant as shown in Fig. 1, where a_p is the depth of cut, F_c, F_f, and F_p are the cutting, feed, and thrust forces, and r_β is the cutting edge radius of the tool. To investigate the effects of tool geometry on forces and residual stresses, Tungsten-Carbide/Cobalt (WC/Co) tools with 3 different edge radii were used. The three levels of edge radii were 5, 10, and 25 μm on average. A coated tool with 10 μm edge radius was also used to measure and simulate the effects of tool coating. A right-hand tool holder (CTFPR-164C) that provides zero lead and side rake angles, $-5°$ back rake angle was used. In addition to three levels of edge radius, two levels of cutting speed ($v_c = 12$ and 24 m/min) were used, at a fixed feed of $f = 0.05$ mm/rev and a depth of cut of $a_p = 1$ mm. Cutting forces were measured with a dynamometer that houses the tool holder. After machining the disks, residual stresses on two orthogonal directions

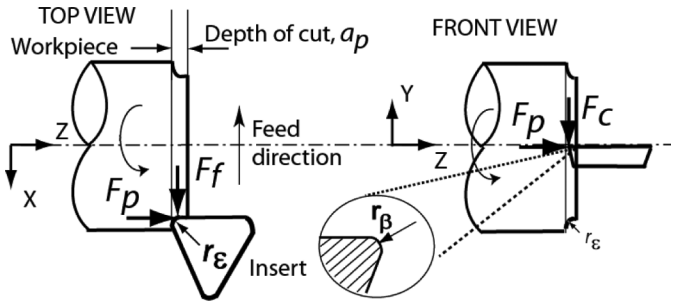

FIGURE 1.—Configuration of face turning experiments [3].

(circumferential and radial) were measured using X-ray diffraction technique on a Proto iXRD unit Mn-Cu-K_α radiation ($\lambda = 2.1$ A°) at 17 kV, 4 mA to acquire {311} diffraction peaks at 2 θ angles of ~155° using a spot size of 1×2 mm beam. To create depth profiles, residual stresses at different levels were measured using electro-polishing to remove successive layers of material after each depth level.

PHYSICS-BASED SIMULATION OF MACHINING

Physics-based finite element simulation models for chip formation has been gaining attention in predicting machining-induced residual stresses and optimization of tool microgeometry and machining parameters without running costly experimentation [2].

In this study, three-dimensional (3-D) chip formation simulation models with continuous remeshing capability are utilized in updated Lagrangian finite element software (DEFORM-3-D). The workpiece and the tool were modeled as viscoplastic (1.5×10^5 element mesh) and rigid (1.0×10^5 element mesh), respectively. A curved uncut workpiece model with a 4 degree segment of disk surface is used, and workpiece end surface is constrained in all directions. Boundary conditions at specified cutting speed were applied to the rigid tool tip model that includes corner radius area and the edge radius [2]. High mesh density was concentrated at the tool tip and around the cutting zone so that detailed output distributions can be obtained (see Fig. 2). Average minimum element sizes for the tool and the workpiece mesh were assigned to 15 µm and 5 µm, respectively.

Heat transfer from workpiece to tool was included with proper thermal boundary conditions where a heat conduction coefficient (h) as 100 kW/m^2/°C was employed. Temperature (T in°C) dependent properties of work and tool material are defined as modulus of elasticity (E in MPa), thermal expansion (α in 1/°C), thermal conductivity (λ in W/m/°C), and heat capacity (c_p in N/mm^2/°C), and are given in Table 1.

In the 3-D finite element model, friction at the tool-chip contact was handled using a hybrid model: (i) shear friction model at sticking contact zone ($m = \tau/k$ k where τ; shear stress, k; shear flow stress, and $m = 0.9$) and (ii) Coulomb friction model at sliding contact zone ($0.6 \leq \mu \leq 0.8$ as friction coefficient).

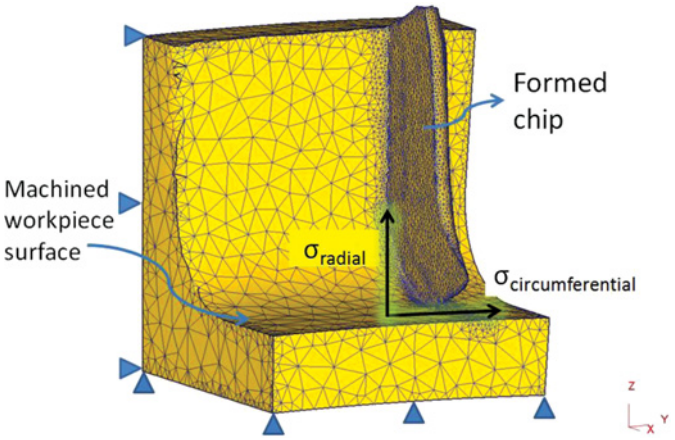

FIGURE 2.—Chip formation in 3D face turning simulation (color figure available online).

Physics-based simulations require a material constitutive model which relates flow stress to strain, strain rate, and temperature. Dynamic flow stress response of nickel-based alloys that was investigated with Split–Hopkinson pressure bar tests operated at various strain rates and temperatures show flow softening behavior [4, 5]. For this reason, a modified material model with flow softening effect in addition to strain and strain rate hardening and thermal softening effects was adopted as given in Eq. (1) [3, 4]:

$$\sigma = [A + B\varepsilon^n]\left[1 + C\ln\frac{\dot{\varepsilon}}{\dot{\varepsilon}_o}\right]\left[1 - \left(\frac{T - T_o}{T_m - T_o}\right)^m\right] \left[D + (1 - D)\left[\tanh\left(\frac{1}{(\varepsilon + p)^r}\right)\right]^s\right], \quad (1)$$

where σ is flow stress, ϵ is true strain, $\dot{\varepsilon}$ is true strain rate, $\dot{\varepsilon}_0$ is reference true strain, and T, T_m, T_o are work, material melting, and ambient temperatures, respectively. The set of model parameters used in the model for IN100 nickel-based alloy are $A = 1{,}350$ MPa, $B = 1{,}750$ MPa, $n = 0.65$, $C = 0.017$, $m = 1.3$, $D = 0.6$, $p = 0$, $r = 1$, $s = 5$, and the melting temperature for IN100 is $T_m = 1{,}490$°C. With these inputs, simulations were executed at the experimental conditions. In Table 2, experimental and simulation results are presented for all 8 cutting conditions in terms of resultant force F $\left(\sqrt{F_c^2 + F_p^2 + F_f^2}\right)$, circumferential and radial

TABLE 1.—Mechanical and thermophysical properties of work and tool materials used in finite element simulations.

	IN100	WC/Co	(Ti, Al)N
$E(T)$	$-61000T + 278000$	5.6×10^5	6.0×10^5
$\alpha(T)$	$10^{-5}e^{0.0849T}$	4.7×10^{-6}	9.4×10^{-6}
$\lambda(T)$	$10.409e^{0.0903T}$	55	$0.0081T + 11.95$
$c_p(T)$	$418.63e^{0.0433T}$	$0.0005T + 2.07$	$0.0003T + 0.57$

TABLE 2.—Summary of finite element simulation on IN100 force and stress predictions ($a_p = 1$ mm and $f = 0.05$ mm/rev).

Variable factors		Experimental results							
			Circumferential		Radial		Combination		
Cutting speed v_c [m/min]	Edge radius r_β [μm]	Force F [N]	Peak tensile PTS_{cm} [MPa]	Peak compressive PCS_{cm} [MPa]	Peak tensile PTS_{rm} [MPa]	Peak compressive PCS_{rm} [MPa]	Peak tensile PTS_m [MPa]	Peak compressive PCS_m [MPa]	St dev σ_{std} [MPa]
12	5	634	868	−264	654	−327	768	−297	52
12	10	610	975	−296	495	−208	773	−256	66
12	25	643	1038	−242	643	−307	863	−276	70
12	C10	617	377	−26	−81	−138	273	−99	56
24	5	700	467	−445	78	−485	335	−465	36
24	10	630	682	−598	217	−490	506	−547	50
24	25	559	830	−372	499	−597	685	−497	54
24	C10	572	800	−39	292	−157	602	−114	43
					Simulation Results				
12	5	625	712	−327	596	−329	657	−328	103
12	10	622	792	−356	379	−343	621	−350	153
12	25	625	849	−374	719	−319	787	−348	310
12	C10	601	356	−131	−53	−144	255	−138	70
24	5	677	454	−304	82	−353	326	−329	122
24	10	632	634	−496	217	−445	474	−471	183
24	25	598	737	−314	466	−312	617	−313	189
24	C10	563	765	−94	253	−112	570	−103	116

peak tensile and peak compressive residual stresses. In addition, a combination of the circumferential and radial direction residual stresses is given, together with a collective uncertainty value for each machining condition. Resultant forces are predicted with very good accuracy (<10% error), whereas the tensile peak residual stresses are underpredicted, and peak compressive residual stresses are overpredicted with reasonable errors (<20%). The uncertainty of the simulation results are significantly more than the experiments, showing the stochastic nature of the simulations.

COMPARISON OF RESIDUAL STRESS PREDICTIONS AND MEASUREMENTS

Finite element simulation predictions in machining IN100 nickel-based super alloy indicated that circumferential residual stresses at the surface increased with increasing cutting speed, while the tool coating/edge radius change did not affect these values (Fig. 3). For both circumferential and radial directions, surface tensile residual stresses showed an increase with increasing cutting edge radius, and the coated tool showed a slightly less surface tensile residual stress than the 25 μm edge radius tool. Compressive peak residual stresses varied from −400 to −600 MPa for the uncoated tools and were not significant for the TiAlN coated tool. Compressive peak residual stresses in circumferential direction were not significant for all tests, but they all showed this peak around 80 μm at approximately −100 MPa. This peak was slightly more compressive with the coated tool compared to the uncoated tool. In the radial direction, all tests exhibited compressive residual stresses both at the surface and deep into the material. The prediction accuracy of the simulations was good in both circumferential and radial directions, and in both low and high cutting speeds ($v_c = 12$ and 24 m/min) (Figs. 3, 4). Measurement and prediction uncertainty in residual stress findings are indicated with standard deviation bars in the same figures.

EXPERIMENTAL AND SIMULATION RESULTS AND MODELING

Experimental and simulation results are represented with a second ordergeneric regression model to form

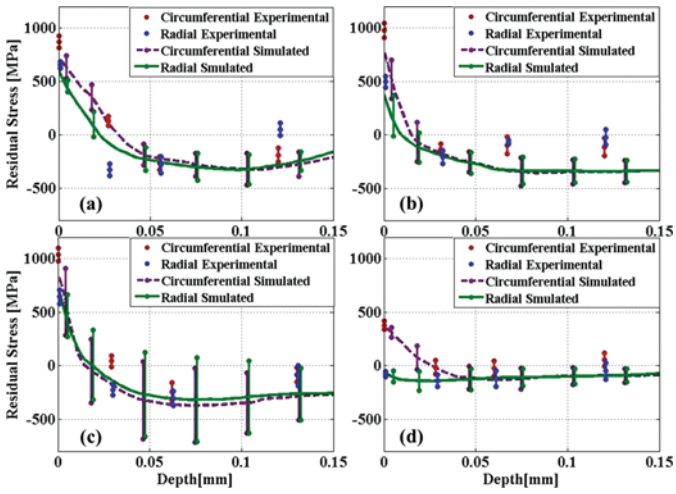

FIGURE 3.—Comparison of residual stresses in face turning of IN100 at $v_c = 12$ m/min with tools: a) Sharp ($r_\beta < 5$ μm), b) $r_\beta = 10$ μm, c) $r_\beta = 25$ μm, and d) TiAlN Coated ($r_\beta = 10$ μm) (color figure available online).

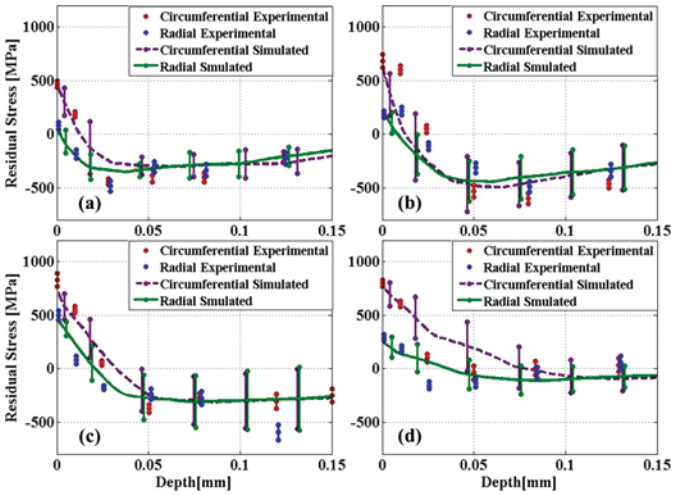

FIGURE 4.—Comparison of residual stresses in face turning of IN100 at $v_c = 24$ m/min with tools: a) Sharp ($r_\beta < 5\,\mu$m), b) $r_\beta = 10\,\mu$m, c) $r_\beta = 25\,\mu$m, and d) TiAlN Coated ($r_\beta = 10\,\mu$m) (color figure available online).

relationships between input and output variables as given in Eq. (2), where βs are the regression coefficients, and ε is the residual error. This generic form is then modified to understand the effects of cutting speed (v_c) and edge radius (r_β) on the outputs such as the resultant F [N], PTS and PCS [MPA], as well as the uncertainty of the measurements and simulations (σ_{std}) [MPa]. Hence, the equations become as Eq. (3), and the resultant coefficients are presented in Table 3. It must be noted that since there are only two levels of cutting speed (v_c), coefficient for the square term that belongs to that input variable (β_{11}) is always zero. The table also shows the R^2 values for each variable that show how good the regression coefficients fit the data, and it can be observed that most of them have over 90% R^2 values:

$$y = \beta_0 + \sum_{i=1}^{k} \beta_i x_i + \sum_{i=1}^{k} \beta_{ij} x_i x_j + \sum_{i=1}^{k} \beta_{ii} x_i^2 + \varepsilon \tag{2}$$

$$F, PTS, PCS, \text{or } \sigma_{std} = \beta_0 + \beta_1 v_c + \beta_2 r_\beta + \beta_{12} v_c^* r_\beta + \beta_{11} v_c^2 + \beta_{22} r_\beta^2 + \varepsilon. \tag{3}$$

MULTIOBJECTIVE PARTICLE SWARM OPTIMIZATION

After validating the simulations with the experiments, it is important to understand how each input parameter affects the forces and surface integrity results, and optimize process parameters accordingly for the most desirable outputs. In order to conduct this optimization, Particle Swarm Optimization (PSO) method [6], an evolutionary computation method similar to genetic algorithms (GAs) is utilized. This technique has been applied to many complex systems in order to find quick solutions for decision making process, including machining systems [7–16]. In this technique, a population of random solutions to the system is first initiated, and then the evolution of these solutions toward the optimal input set is observed over generations. Different than GA, PSO particles do not die or mutate, but instead move in the decision variable space freely with velocities that change over generations. PSO is still considered to be a derivative of GAs and is utilized in many different optimization problems in various fields [17, 18]. In multiobjective PSO (MOPSO), there is more than one objective, so it is possible to result in more complex Pareto fronts. However, the results have to be nondominated, which means no optimal solution can have higher values in all dimensions than any other optimal solution. When the initial population is generated, each particle is assigned a position and a velocity in the decision variable space. By considering previous position and current velocity of particles, a new particle position is found at every generation (Eq. 4). Accordingly, particle velocity is updated by considering previous velocity and

TABLE 3.—Model parameters for the response.

Variable Factors	Experimental results							
			Circumferential		Radial		Combination	
	F	PTS_{cm}	PCS_{cm}	PTS_{rm}	PCS_{rm}	PTS_m	PCS_m	σ_{std}
β_0	585	1069	206	1289	−248	1105	−28	48.9
β_1	8.24	−34.8	−22.2	−48.5	−14.5	−36.8	−17.8	−1.34
β_2	−4.42	38	−46.3	−42.3	32.9	7.31	−6.27	4.48
β_{12}	0.40	−1.26	1.39	0.82	−0.91	−0.43	0.25	−0.12
β_{22}	−0.61	0.73	0.38	1.56	−0.43	0.93	−0.079	0.0028
R^2	99.82	99.49	93.93	95.94	97.57	98.34	95.47	100.00
				Simulation Results				
β_0	595	792	−17.6	1087	−132	873	−72.9	−74.7
β_1	5.02	−21.7	−6.58	−35.4	−6.49	−24.4	−6.67	6.53
β_2	−2.23	32	−49.5	−42	−26.8	3.16	−38.3	26.9
β_{12}	0.19	−1.03	1.38	1.39	0.79	−0.05	1.08	−0.28
β_{22}	−0.30	0.53	0.38	0.72	0.24	0.48	0.32	−0.64
R^2	95.76	98.72	63.53	90.93	81.03	95.04	69.27	97.59

acceleration terms (Eq. 5), where, x_i^k is the position, v_i^k is the velocity for particle i at generation k, $pbest_i$ is the best personal solution of particle i, $gbest$ is the best global solution ever encountered throughout population, c_i are the fixed acceleration terms for the personal and global bests, $rand_i$ are the random numbers in [0, 1] to introduce stochastic effects of acceleration terms, w is the weighting function for the previous velocity term, and δ is a random number in [−1, 1] used in avoiding local minima. The random values were determined separately for each coordinate, as these coordinates are independent from each other. At the initial steps, w is set at a relatively higher value to make sure the initial accelerations do not spread all the particles in the decision variable space. At the later generations, this value is decreased so that the particles can have more freedom in searching for possible better solutions, while the global best is stored. At each generation, the objective functions are computed for the current positions, and if personal or global best values change, they are updated. These generations are stopped when the algorithm reaches a predetermined iteration number, or there is no further movement of *pbest* values of the particles. At each generation, when the velocities are updated, velocities are bounded in predetermined maximum and minimum values in order to prevent uncontrolled increase in velocities that causes instabilities in the search algorithm. Likewise, particle positions can never leave the decision variable space boundaries:

$$x_i^{k+1} = x_i^k + v_i^{k+1} \tag{4}$$

$$v_i^{k+1} = \omega v_i^k + c_1 rand_1\left(pbest_i - x_i^k\right) + c_2 rand_2\left(gbest - x_i^k\right) + \delta. \tag{5}$$

After constructing the algorithm, the objective functions are created, namely, as minimizing the resultant forces, the tensile peak of the residual stress curve on the surface (*PTS*), the compressive peak of the residual stress curve (*PCS*), and the total uncertainty related to these values, which represents the amount of confidence involved in the measurements or simulations. Of the four different objectives, three were selected at each trial to illustrate the results in three dimensional graphs. Once the objectives are set, the minimization algorithm given in Eq. (6) is utilized to optimize the solution population, where $f_1(x)$, $f_2(x), \ldots,$ $f_k(x)$ represent the aforementioned objective functions, $g_j(x)$, $h_j(x)$ are the constraints and process limitations with a set of decision variables ($x = x_1, \ldots,$ x_n) (i.e., n number of process parameters), and $\mathbf{X}$ is the space with all feasible solutions.

Minimize (or maximize)

$$\{f_1(x), f_2(x), \ldots, f_k(x)\} \text{subject to}$$

$$g_j(x) \le b_j \text{ for } j = 1, 2, \ldots, m, \tag{6}$$

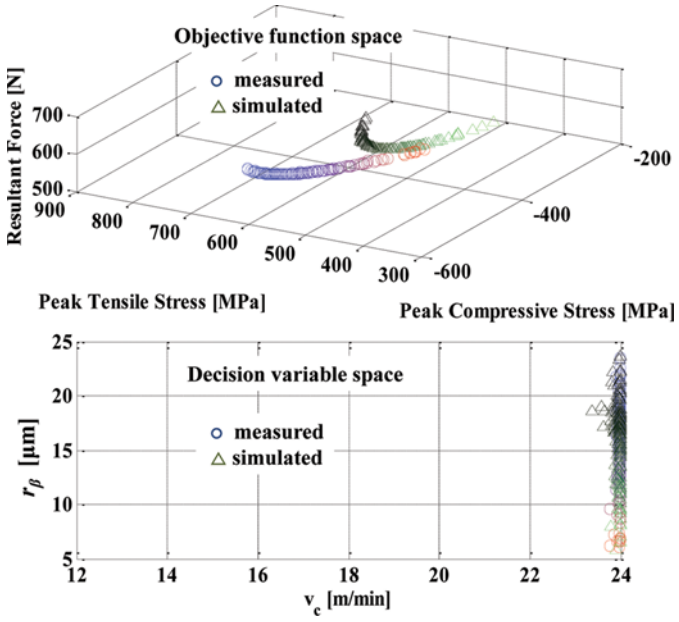

FIGURE 5.—Comparison of optimum solutions for minimizing measured and simulated stresses with minimizing resultant force (color figure available online).

and

$$h_j(x) = b_j \text{ for } j = m+1, .., m+p, x \in \mathbf{X}$$

Therefore, Pareto fronts for minimizing three objective functions (*F, PTS*, and *PCS*) are given with comparisons of objective functions that are obtained from measured and simulated residual stresses are given in Fig. 5. In this proposed multiobjective optimization, each simulation with a population size of 1,000 runs about

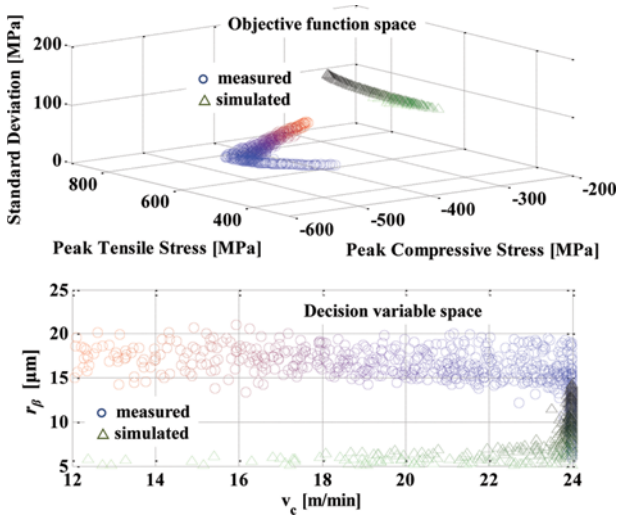

FIGURE 6.—Comparison of optimum solutions for measured and simulated stresses with minimizing standard deviation (color figure available online).

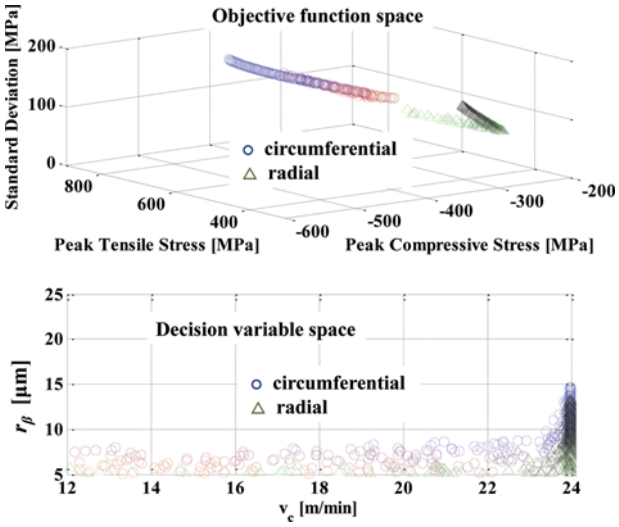

FIGURE 7.—Comparison of optimum solutions for circumferential and radial stresses with minimizing standard deviation (color figure available online).

20 minutes on a PC with Pentium Dual Core processor until reaching an acceptable solution. Simulation experiments were run to identify most optimum setting of MOPSO parameters. Optimum solution for minimizing all three objectives has occurred at the cutting speed $v_c = 24\,\mathrm{m/min}$ where a small edge radius provides minimum resultant force. In addition, Pareto fronts for minimizing another three objective functions (*STD, PTS*, and *PCS*) are given in Fig. 6. In dealing with minimizing standard deviation, objective functions obtained from measured residual stresses provide optimum solutions of an edge radius of $15\,\mu\mathrm{m} < r_\beta < 20\,\mu\mathrm{m}$ with a higher cutting speed of $v_c > 20\,\mathrm{m/min}$. Finally, Pareto fronts for minimizing objective functions (*STD, PTS*, and *PCS*) are given with comparisons of simulated circumferential and radial residual stresses in Fig. 7. In this case, the optimum solution is obtained for minimizing both simulated and predicted stresses and the standard deviation at the cutting speed $v_c = 24\,\mathrm{m/min}$ as well. It should be noted that most optimal solutions were obtained at or near the boundaries of decision variable space.

CONCLUSIONS

This study presents investigations on machining induced residual stresses in IN100 nickel-based alloy material with multiple objectives in minimizing *F, PTS*, and *PCS*. In addition, minimizing standard deviation is also utilized as an additional objective to remedy uncertainty in measurements and physics-based simulation predictions. MOPSO that can handle three objectives simultaneously is employed, and solutions in objective function and decision variable spaces are obtained. The results indicate that simulations validated with experiments present a viable alternative in identifying optimum machining parameters.

ACKNOWLEDGMENT

This work was supported by National Science Foundation grant NSF-CMMI-1130780.

REFERENCES

1. Ulutan, D.; Özel, T. Machining induced surface integrity in titanium and nickel alloys: A review. *International Journal of Machine Tools and Manufacture* **2011**, *51*, 250–280.
2. Jawahir, I.S.; Brinksmeier, E.; M'Saoubi, R.; Aspinwall, D.K.; Outeiro, J.C.; Meyer, D.; Umbrello, D.; Jayal, A.D. Surface integrity in material removal processes: Recent advances. *CIRP Annals–Manufacturing Technology* **2011**, *60*, 603–626.
3. Özel, T.; Ulutan, D. Prediction of machining induced residual stresses in turning of titanium and nickel based alloys with experiments and finite element simulations. *CIRP Annals–Manufacturing Technology* **2012**, *61*, 547–550.
4. Ulutan, D.; Sima, M.; Özel, T. Prediction of machining induced surface integrity using elastic-viscoplastic simulations and temperature-dependent flow softening material models in titanium and nickel-based alloys. *Advanced Materials Research* **2011**, *223*, 401–410.
5. Zhang, J.M.; Gao, Z.Y.; Zhuang, J.Y.; Zhong, Z.Y.; Janschek, P. Strain-rate hardening behavior of superalloy IN71. *Journal of Materials Processing Technology* **1997**, *70*, 252–257.
6. Eberhart, R.C.; Kennedy, J. Particle Swarm Optimization. In *Proceedings of IEEE International Conference on Neural Networks*, Piscataway, NJ, 1995; 1942–1948.
7. Karpat, Y.; Özel, T. Multi-objective optimization for turning processes using neural network modeling and dynamic-neighborhood particle swarm optimization. *International Journal of Advanced Manufacturing Technology* **2007**, *35* (3–4), 234–247.
8. Vázquez, E.; Ciurana, J.; Rodríguez, C.A.; Thepsonthi, T.; Özel, T. Swarm intelligent selection and optimization of machining system parameters for micro-channel fabrication in medical devices. *Materials and Manufacturing Processes* **2011**, *26* (3), 403–414.
9. Thepsonthi, T.; Özel, T. Multi-objective process optimization for micro-end milling of Ti-6Al- 4 V titanium alloy. *International Journal of Advanced Manufacturing Technology* **2012**, *63* (9–12), 903–914.
10. CoelloCoello, C.A.; Becerra, R.L. Evolutionary multiobjective optimization in materials science and engineering. *Materials and Manufacturing Processes* **2009**, *24* (2), 119–129.
11. Hu, X.; Eberhart, R. Multiobjective optimization using dynamic neighborhood particle swarm optimization. In *Proceedings of the 2002 Congress on Evolutionary Computation*, Honolulu, HI, May 12–17, 2002; 1677–1681.
12. CoelloCoello, C.A., Pulido, G.T.; Lechuga, M.S. Handing multi-objectives with particleswarm optimization. *IEEE Transactions on Evolutionary Computation* **2004**, *8* (3), 256–279.
13. Mostaghim, S.; Teich, J. Strategies for finding good local guides in multi-objective particle swarm optimization (MOPSO). In *IEEE Swarm Intelligence Symposium Proceedings*, Indianapolis, IN, April 2003; 26–33.
14. Agrawal, S.; Dashora, Y.; Tiwari, M.K.; Son, Y.J. Interactive particle swarm: A Pareto-adaptive Metaheuristic to

multi-objective optimization. *IEEE Transaction on System, Man and Cybernetics–Part A: System and Human* **2008**, *38* (2), 258–277.

15. Tripathi, P.K.; Bandyopadhyay, S.; Pal, S.K. Adaptive multi-objective particle swarm optimization algorithm. In *Proceedings of the IEEE Congress on Evolutionary Computation (CEC2007)*, Singapore, 2007; 2281–2288.
16. Zielinski, K.; Laur, R. Adaptive parameter setting for a multi-objective particle swarm optimization algorithm. In *Proceedings of the IEEE Congress on Evolutionary Computation (CEC2007)*, Singapore, 2007; 3019–3026.
17. Chakraborti, N.; Jayakanth, R.; Das, S.; Calisir, E.A.; Erkoc, S. Evolutionary and genetic algorithms applied to Li + -C system: Calculations using differential evolution and particle swarm algorithm. *Journal of Phase Equilibria and Diffusion* **2007**, *28* (2), 140–149.
18. Chakraborti, N.; Das, S.; Jayakanth, R.; Pekoz, R.; Erkoc, S. Genetic algorithms applied to Li + ions contained in carbon nanotubes: An investigation using particle swarm optimization and differential evolution along with molecular dynamics. *Materials and Manufacturing Processes* **2007**, *22* (5–6), 562–569.